Pergamon

Atmospheric Environment Vol. 28, No. 5, pp. 873–887, 1994
Elsevier Science Ltd

1352-2310/94 $6.00 + 0.00

RADIOMETRIC MODEL OF THE TRANSMISSION CELL-RECIPROCAL NEPHELOMETER

GEORGE W. MULHOLLAND and NELSON P. BRYNER
National Institute of Standards and Technology, Gaithersburg, MD 20899, U.S.A.

Abstract—A radiometric model has been developed to assess the effects of angular truncation, finite size of the detector, and angle response characteristics of the cosine sensor on the measurement of the total scattering coefficient by a transmission cell-reciprocal nephelometer. These effects are computed for monodisperse polystyrene spheres over the size range 0.02–8 μm based on Mie theory and for smoke agglomerates ranging from 10 to 10^7 primary units based on the Fisher–Burford approximation. The accuracy of the model calculations is determined by comparison with exact solutions for the case of a detector with an infinitesimal area and for a finite area detector with a diffuse scattering function. The predicted results are compared with measured results for six different sizes of monodisperse polystyrene sphere aerosols with particle diameters in the range 0.1–2.35 μm. The measurements were carried out as a function of the distance between the laser beam and detector for 1.3 and 2.7 cm diameter cosine sensors. A table of design parameters for making accurate total scattering measurements is obtained for both spheres and agglomerates. An accuracy of $\pm 5\%$ was obtained for spherical particles with diameters $\leqslant 1.1$ μm with our TCRN, and we estimate that similar performance would be obtained for smoke agglomerates with up to 3×10^3 primary spheres per agglomerate.

Key word index: Absorption coefficient, aerosol, agglomerates, extinction coefficient, nephelometer, scattering coefficient, smokes.

1. INTRODUCTION

The optical properties of combustion-generated aerosols, which we shall refer to as smoke, are of concern in regard to the degradation of visibility in pristine areas, to the global climatic impact of a major nuclear exchange, as well as the localized climatic impact of forest fires and oil well fires such as those recently extinguished in Kuwait. There is a large uncertainty in the optical properties of smokes including the scattering and absorption coefficients per unit concentration of smoke and the single scattering albedo, defined as the ratio of the total scattering coefficient to the extinction coefficient. A comparison study (Gerber and Hinaman, 1982) involving simultaneous measurements of the optical properties of smoke generated from the combustion of propane resulted in values ranging from 3.8–11.4 $m^2 g^{-1}$ for the absorption coefficient and 0.09–0.29 for the single scattering albedo.

Gerber (1979, 1982) developed an instrument for simultaneously measuring the light extinction coefficient σ_{ext} and the total scattering coefficient σ_s of ambient atmospheric aerosols with a multi-pass optical cell. From these measurements, the single scattering albedo is obtained as the ratio σ_s/σ_{ext} and the light absorption coefficient is obtained as the difference $\sigma_{ext} - \sigma_s$. The total scattering measurement in Gerber's instrument utilizes a diffuser before the detector and is the inverse of traditional nephelometry (Charlson *et al.*, 1967), which uses a diffuser to provide a cosine distribution of the light source. We use the term transmission cell-reciprocal nephelometer (TCRN) to describe this instrument. Patterson *et al.* (1991) developed a single-pass TCRN and used it to characterize the optical properties of smoke generated by the combustion of lumber, various plastics, petroleum products, and tire rubber.

This paper assesses the accuracy of the TCRN for the total scattering measurement through a combination of modeling and measurement. The model calculations consist of computing the total flux of light scattered from particles in a laser beam to the cosine corrected sensor/detector in the TCRN. We compute the effects of the finite area of the sensor, the limited acceptance angle, and the non-ideal sensor performance on the TCRN performance as a function of particle size for polystyrene spheres and smoke agglomerates. The predictions of the radiometric model are compared with measurements. Of special interest is the predicted performance of the instrument for large smoke agglomerates, which might be produced in the atmosphere as a result of large scale fires such as the oil well fires in Kuwait (Johnson *et al.*, 1991).

2. RADIOMETRIC MODEL FOR TCRN

The schematic in Fig. 1 illustrates light scattered from an incremental scattering volume, δv, to an infinitesimal area a_1 of a circular detector located a distance s from the scattering volume. The basic quantity of interest is F_{ij}, the flux of light scattered from volume element i to detector element j. The flux F_{ij} is proportional to the light scattered from element

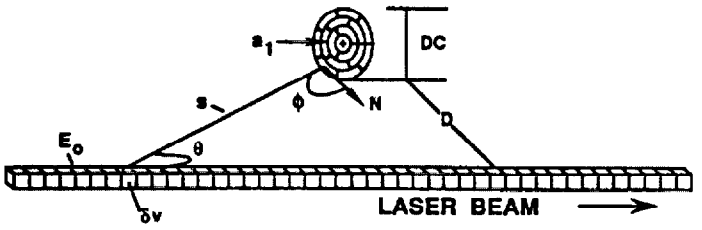

Fig. 1. Geometrical arrangement of laser beam and detector in the TCRN with DC the diameter of the detector, a_1 the area of a sector, and E_0 the incident laser irradiance.

i in the direction θ, $I(\theta)$, and to the projected area $a_1 \cos\phi$ of the detector element, and inversely proportional to s^2.

$$F_{ij} = I(\theta) a_1 \cos\phi / s^2 \tag{1}$$

where s, θ, and ϕ all, of course, depend on i and j. This expression assumes all the light flux incident on the projected area of the detector element is detected. The change in the analysis for an actual detector system are considered below.

The scattering intensity $I(\theta)$, which is defined as the scattered flux per solid angle, is equal to the product of the laser irradiance E_0, the volumetric scattering coefficient $\sigma(\theta)$, and the scattering volume δv.

$$I(\theta) = E_0 \sigma(\theta) \delta v. \tag{2}$$

The volumetric scattering coefficient has dimension $m^{-1} sr^{-1}$ and $I(\theta)$ has dimension $W sr^{-1}$.

As the laser beam propagates through the smoke, the laser intensity will decrease. There will also be a decrease in intensity of the scattered light as it travels the distance s from the scattering volume to the detector. The combined effect will be to reduce the scattering intensity by a factor P given by Bouguer's law as

$$P = \exp(-\sigma_{ext} s_t) \tag{3}$$

where σ_{ext} is the extinction coefficient of the aerosol and s_t is the total pathlength of the light through the uniformly distributed smoke.

$$s_t = s + x + L/2. \tag{4}$$

The cell length is L; the origin of the coordinate system is the center of the laser beam at the midpoint of the cell so that x corresponds to the coordinate along the laser beam. The center of the cosine sensor is at $z = D$, $x = 0$, and $y = 0$. This light extinction correction is valid for low concentration aerosols for which there is little multiple scattering. Substituting from equation (2) into equation (1) and multiplying the right-hand side of equation (1) by P as expressed in equation (3), we obtain

$$F_{ij} = \frac{E_0 \sigma(\theta) \delta v a_1 \cos\phi \exp(-\sigma_{ext} s_t)}{s^2}. \tag{5}$$

The scattered light received by the sensor is equal to the sum of F_{ij} over i and j, where j refers to the sum over the sensor surface elements and i to the sum over the elements in the length of the laser beam in the cell. In performing the double summation, it is convenient to divide the circular sensor into sector elements, as illustrated in Fig. 2. The concentric circles have radii r_{J1}

$$r_{J1} = J1 r_0 \tag{6}$$

where r_0 refers to the radius of the inner circle. Annular ring $J1$ is divided up into $J2$ sectors

$$J2 = 2(J1) - 1. \tag{7}$$

The inner circle is considered the first annular region with one element $J2 = 1$, the second annular region is divided every 120° into three elements $J2 = 3$, the third annular region every 72° into five elements $J2 = 5$, and so on. This method of dividing the disk insures that every sector has the same area a_1 given by

$$a_1 = \pi r_0^2 = \frac{\pi DC^2}{4 J1_{max}^2} \tag{8}$$

where DC is the diameter of the detector. The second equality is based on the total number of sectors being equal to the square of the total number of circles $(J1_{max})^2$.

We can now express the total flux F from the laser beam to the detector as a triple sum over the elements *I of the laser beam and elements indexed by* $J1$ *and* $J2$ over the area of the detector. Neglecting the light extinction correction and expressing δv in terms of dx,

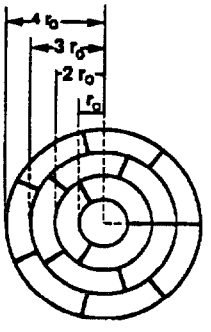

RING NUMBER J1	NUMBER OF SECTORS J2
1	1
2	3
3	5
4	7
N	2N - 1

Total Number of Sectors = N^2

Fig. 2. Discretization of the circular sensor into equal area sectors.

dy and dz, we obtain the following expression for F

$$F = E_0\,dx\,dy\,dz\,a_1 \sum_{I=1}^{I_m} \sum_{J1=1}^{J1_{max}} \sum_{J2=1}^{2J1-1} \frac{\sigma(\theta)\cos\phi}{s^2} \quad (9)$$

where s, θ, and ϕ can be expressed in terms of the following:

$X_c(J1, J2)$ is the x coordinate of disk
$Y_c(J1, J2)$ is the y coordinate of disk
$X(I)$ is the x coordinate along laser beam
$XA = X_c(J1, J2) - X(I)$
D is the distance from laser beam to the disk.

$$s^2 = D^2 + Y(J1, J2)^2 + XA^2 \quad (10)$$

$$\cos\phi = \frac{D}{s} \quad (11)$$

$$\cos\theta = \frac{[XA^2 + Y(J1, J2)^2]^{1/2} XA}{s|XA|}. \quad (12)$$

At this point we omit the effect of the light extinction correction to allow comparison with exactly solvable cases. In Section 7 the effect of the light extinction correction is discussed.

The scattering function $\sigma(\theta)$ depends on the direction of polarization of the incident light. We are interested in the case of unpolarized or natural light, which can be treated as the sum of two orthogonal, equal amplitude, linearly polarized waves. This is equivalent to a laser light source polarized at 45° relative to the plane defined by the laser beam and the center of the detector. The fact that the laser light is coherent does not affect the results for the case of time-averaged scattering from randomly moving particles.

The polarization direction of the incident laser will not be 45° relative to the plane defined by a point displaced vertically from the center of the detector and the laser. In Fig. 3 we show the direction of polarization and a projection of the scattering plane for one point above the center of the detector at angle α and another point an equal distance below the center of the detector. In Appendix A, it is shown that the sum of the scattered light intensities for these two points is independent of the angle α for spherical particles and for randomly oriented non-spherical particles. In other words, the effective polarization direction is 45° for pairs of points. Our discretization shown in Fig. 2 is arranged so that for every sector with a $+y$ coordinate there is a corresponding sector with a $-y$ coordinate.

It is of interest to consider two special cases of equation (9) for which there are exact results. The first case is for a detector with an infinitesimal area. This case provides a direct connection between the measured flux and the total scattering coefficient. The second is for the flux from a point light source to a finite area detector. This second case provides a check on the truncation error in our numerical integration.

2.1. *Infinitesimal detector area*

For the case of an infinitesimal detector area, the triple sum reduces to a single sum over the length L of the laser beam within the cell. Referring to Fig. 4 and noting that $\tan\phi = x/D$, one finds that dx can be expressed in terms of $d\phi$, where ϕ is defined by the scattered ray and the normal to the detector's surface

$$dx = \frac{s^2\,d\phi}{D}. \quad (13)$$

Substituting for dx from equation (13) into equation (9), converting from a sum over L to an integral over ϕ, and neglecting the beam extinction effect, one obtains the following expression for the total flux F from the laser beam to the incremental detector surface a_1

$$F = \frac{E_0\,dy\,dz\,a_1}{D} \int_{-\pi/2}^{\pi/2} \sigma(\theta)\cos\phi\,d\phi. \quad (14)$$

The angular limits correspond to the laser beam extending from $x = -\infty$ to $x = +\infty$.

The total scattering coefficient σ_t is defined as follows:

$$\sigma_t = \int \sigma(\omega)\,d\omega = \int_0^{2\pi} \int_0^{\pi} \sigma(\theta, \psi)\sin\theta\,d\theta\,d\psi. \quad (15)$$

The angle θ is the scattering angle defined by the direction of propagation of the incident beam and the direction of the scattered beam, and ψ is the azimuthal angle varying from 0 to 2π for fixed θ. The scattering function for spheres is only a function of θ. For non-spherical particles, the orientation averaged scattering

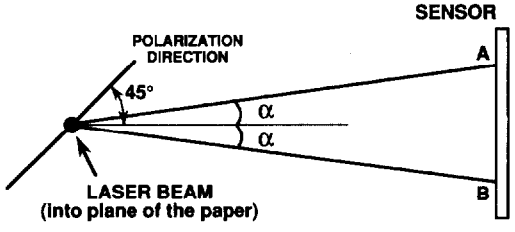

Fig. 3. Illustration of the laser polarization direction and the scattering direction for points A and B on the detector as viewed down the laser beam.

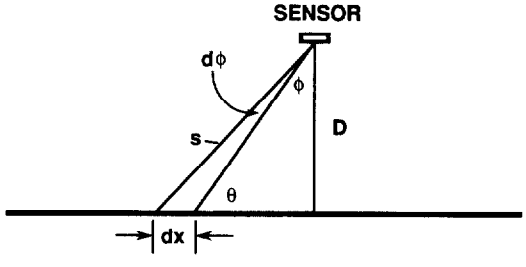

Fig. 4. Diagram showing relationship between dx and $d\phi$ with ϕ the angle defined by the scattering direction and the normal to the sensor.

function $\sigma_0(\theta)$ is also a function of θ only. So for these two cases, the total scattering σ_t reduces to

$$\sigma_t = \int_0^{2\pi}\int_0^{\pi} \sigma_o(\theta)\sin\theta\,d\theta\,d\psi = 2\pi\int_0^{\pi}\sigma_o(\theta)\sin\theta\,d\theta. \quad (16)$$

The integral in equation (14) can be expressed in terms of the scattering angle θ. The range for θ is 0–π, while the range for ϕ is $-\pi/2$–$+\pi/2$, so that the angle ϕ illustrated in Fig. 4 has a negative value. This is important in deriving the following trigonometric relation

$$\theta = \phi + \pi/2. \quad (17)$$

From equations (14) and (17), we obtain F as an integral over θ

$$F = \frac{E_o\,dy\,dz\,a_1}{D}\int_0^{\pi}\sigma_o(\theta)\sin\theta\,d\theta. \quad (18)$$

Using equation (16), F can be expressed in terms of σ_t as

$$F = \frac{E_o\,dy\,dz\,a_1\,\sigma_t}{2\pi D}. \quad (19)$$

This relation is valid for the two types of particles described above: spheres and the orientation-averaged total scattering for non-spherical particles. The general relation between total scattering coefficient and detector flux was first presented by Beutell and Brewer (1949) and the derivation given above is similar to that presented by Gerber (1979). Equation (19) is the basis for using the TCRN for determining the total scattering coefficient.

2.2. *Light flux from a point source to a disk*

To determine the truncation error in carrying out the sum over the surface of the detector, we compare our numerical result with the exact solution for the case of the light flux F_{dc} from an incremental area with radiance E_c to a circular disk detector. In this case the radiant flux to the detector is proportional to the projected area of the source, $dx\,dy\cos\phi$. The constant radiance source corresponds to a volumetric differential scattering coefficient proportional to $\cos\phi$. The solution for this case is obtained from an exact solution of the inverse problem of light emitted from a radiating circular disk (Foote, 1916) and the reciprocity relation (Siegel and Howell, 1981) between the radiant flux from a source to a detector and the flux computed for the position of the source and detector interchanged.

$$F_{dc} = \frac{\pi}{2}E_c\,dx\,dy \times\left[1 - \frac{x^2+D^2-a^2}{[(x^2+D^2)^2+2a^2(D^2-x^2)+a^4]^{1/2}}\right] \quad (20)$$

where $dx\,dy$ is the infinitesimal area and a is the radius of the disk. For the case where $dx\,dy$ is directly below the center of the disk, $x=0$, equation (20) reduces to the following

$$F_{dc} = \pi E_c\,dx\,dy\left[\frac{a^2}{D^2+a^2}\right]. \quad (21)$$

A qualitative estimate of the effect of the finite size of the detector on the flux reaching the detector can be made from equation (21). For the case of a detector radius much smaller than D, the flux is inversely proportional to D^2. For the case that a/D equals 0.5, neglecting the a^2 term in equation (21) will result in a 25% overestimate in the flux. The basic reason that the flux per area is smaller for a finite area detector is the increased distance s for a point off the centerline of the detector. So, in general, the finite size effect will result in an underestimate of the scattering coefficient.

We determine the truncation error in using the sum over the detector area given by equation (9) by comparing with the exact result given by equation (21). We compute the reduced flux F_r from the point $x=0$ to the detector for the case $a/D=0.5$ as a function of $J1_{max}$ using equation (9) with $\sigma = E_c\cos\phi$.

$$F_r = \frac{F}{E_0\,dx\,dy\,dz}. \quad (22)$$

From equation (21), we compute the exact expression for the reduced flux F_{re} for this case as

$$F_{re} = \frac{F_{dc}}{E_c\,dx\,dy} = \frac{\pi}{5}. \quad (23)$$

The slight difference in the reduced functions is that equation (22) was derived based on volumetric scattering while the exact solution is based on a specified surface radiance. The fractional error δF is found to be inversely proportional to the total number of sectors.

$$\delta F = \frac{F_r - F_{re}}{F_{re}} \simeq \frac{0.1}{\text{No. of sectors}}. \quad (24)$$

For the case where the detector is divided into 10 annular rings resulting in 100 sectors, the fractional error is about 0.001. Subsequent calculations were carried out for the number of rings $J1_{max}$ greater than or equal to 10.

3. SCATTERING FUNCTIONS

In this study we focus on two types of particles: polystyrene spheres, which are of interest for calibrating the TCRN, and smoke agglomerates, for which there is a need for accurate optical property data.

3.1. *Spheres*

The differential scattering cross sections for spheres, $\sigma_v(\theta)$ and $\sigma_h(\theta)$, are computed based on Mie theory. The v and h subscripts refer to the direction of polarization of the incident light. The dimension of σ for a single sphere is (length)^2, while above we were con-

sidering the scattering per unit volume with dimension (length)$^{-1}$. The average of $\sigma_v(\theta)$ and $\sigma_h(\theta)$, $\sigma_s(\theta)$, is equivalent to the differential cross-section for unpolarized light.

$$\sigma_s(\theta)=1/2(\sigma_v(\theta)+\sigma_h(\theta)). \tag{25}$$

The scattering calculations are carried out for the He–Ne wavelength, $\lambda=632.8$ nm, for polystyrene spheres with refractive index m equal to 1.588, and for particle diameters of 0.0175, 0.100, 0.234, 0.305, 0.60, 1.101, 2.35, 4.0 and 8.0 μm. The diameters from 0.100 to 2.35 μm correspond to the diameters of monodisperse polystyrene spheres for which measurements were made. The values of $\sigma_s(\theta)$ is computed in 1° increments from 0 to 180° and stored in an array for use in the radiant flux calculation (equation (9)). The differential scattering plots for $\sigma_s(\theta)$ in Fig. 5 show the increasing contribution of the near forward scattering as the particle size is increased from 0.234 to 4.0 μm.

3.2. *Smoke agglomerates*

Smoke agglomerates are made of nearly uniform size spherules with a diameter on the order of 0.02–0.04 μm (Samson *et al.*, 1987). The light scattering by computer generated agglomerates has been calculated by Mountain and Mulholland (1988). They express the differential scattering cross-section of an agglomerate σ_{ag} as a product of the scattering function of a primary unit S_r and the structure factor of the agglomerate S_{ag}.

$$\sigma_{ag}=S_r S_{ag}. \tag{26}$$

The quantity S_r corresponds to Rayleigh scattering from a sphere.

$$S_r=\tfrac{1}{2}k^4|\alpha|^2(1+\cos^2\theta). \tag{27}$$

The quantity k is the wavenumber $2\pi/\lambda$ and α is the polarizability. For the scattering from the agglomerates, we use the Fisher–Burford form (1967), which Mountain and Mulholland found to have the same features as their calculations for simulated smoke agglomerates, namely

$$S_{ag}=\frac{N^2}{[1+2(R_g q)^2/3D_f]^{D_f/2}} \tag{28}$$

where q is related to the scattering angle θ and wavelength of light λ by the expression

$$q=\frac{4\pi}{\lambda}\sin(\theta/2). \tag{29}$$

This expression is based on a fractal structure with fractal dimension D_f.

This choice of scattering function is adequate for a first order assessment of the TCRN response to smoke agglomerates. More quantitative models (Nelson, 1989b; Drolen *et al.*, 1987; Iskander *et al.*, 1989), which include multiple scattering have been developed; however, they are computationally intensive and results are limited to agglomerates with fewer than 1000 spheres. The calculations of Nelson (1989a) indicate that multiple scattering may have a small effect in the case of low density smoke agglomerates.

The quantity R_g, the radius of gyration, is defined as the second moment of the mass distribution of the agglomerate

$$m_t R_g^2=\sum_{i=1}^{n} m_i r_i^2 \tag{30}$$

where m_t is the total mass of the agglomerate and m_i is the mass of particle i whose center is at a distance r_i from the centroid. A key characteristic of a fractal object is the power law relationship between the number N of primary units in an agglomerate and the radius of gyration, R_g

$$N=k(R_g/d_p)^{D_f} \tag{31}$$

where d_p is the diameter of the primary sphere. The fractal dimension D_f is defined by this equation.

Using equation (26)–(29), we can express σ_{ag} in the following form

$$\sigma_{ag}(\theta)=\frac{AN^2(1+\cos^2\theta)}{\left[1+\frac{2}{3D_f}[R_g(4\pi/\lambda)\sin(\theta/2)]^2\right]^{D_f/2}} \tag{32}$$

where

$$A=\frac{1}{2}k^4|\alpha|^2. \tag{33}$$

This expression for $\sigma_{ag}(\theta)$ is substituted into equation (9) to compute the total flux reaching the detector. An important feature of the expression for σ_{ag} is that it can be integrated exactly over solid angle (see equation (15)) to give the total scattering σ_{ag}^t. To perform the integration, one expresses the integrand in terms of $\sin^2(\theta/2)$. The final result is given by

$$\sigma_{ag}^t=\frac{8AN^2}{b}\left[\frac{1+2/b+2/b^2}{1-D_f/2}[(1+b)^{1-D_f/2}-1]\right.$$

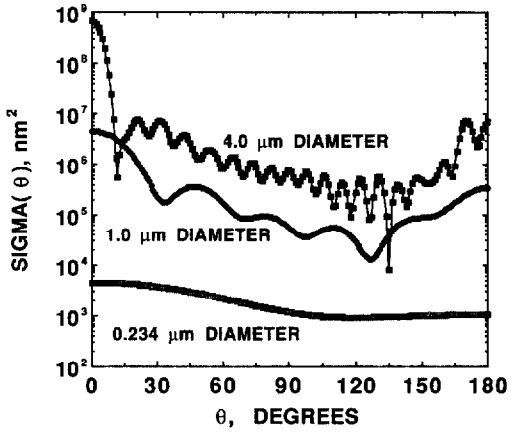

Fig. 5. Scattering cross-section for unpolarized, $\sigma_s(\theta)$, is plotted vs scattering angle for polystyrene spheres with refractive index = 1.588 and $\lambda=632.8$ nm. The results are calculated at 1° intervals from 0 to 180° for the TCRN.

$$-\frac{2/b+4/b^2}{2-D_f/2}[(1+b)^{2-D_f/2}-1] + \frac{2}{b^2(3-D_f/2)}[(1+b)^{3-D_f/2}-1]\Bigg] \quad (34)$$

where b is defined as follows

$$b=\frac{2}{3D_f}[R_g(4\pi/\lambda)]^2. \quad (35)$$

The quantities σ_{ag}^1 and $\sigma_{ag}(\theta)$ are computed for the case of fractal agglomerates with $D_f=1.9$, proportionality constant k (equation (31))$=5.8$, $\lambda=632.8$ nm, primary particle size $d_p=30$ nm, and refractive index $n=1.7$–$0.68i$. The calculations were carried out for 7 agglomerates sizes, 10, 10^2, 10^3, 10^4, 10^5, 10^6, 10^7 primary spheres.

As can be seen from equation (28), the differential scattering is proportional to N^2 at small angles and then varies as q^{-D_f} for large q, or equivalently for large angles. There are no pronounced oscillations in the scattering pattern as in the case for the sphere. As the agglomerates increase in size, the light scattering becomes more intense in the forward direction as illustrated in Fig. 6.

4. RESULTS FOR PERFECT COSINE SENSOR

Implicit in the model is the assumption that the light received by the detector is proportional to the projected area of the sensor. This is the case for a perfect cosine sensor. Such a condition is approached for the case of light entering the aperture of an integrating sphere. In this section we assume a perfect cosine sensor; in the next section we consider a physical model of an actual cosine corrected sensor such as used in the TCRN.

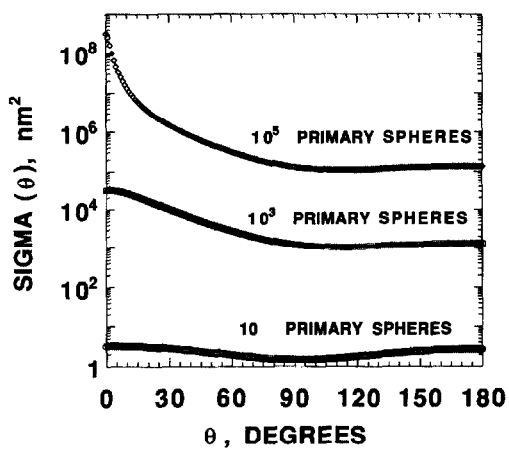

Fig. 6. Scattering cross-section for unpolarized light, $\sigma_{ag}(\theta)$, is plotted vs scattering angle for agglomerates with fractal dimension of 1.9, prefactor 5.8, refractive index of 1.7–0.68i, $\lambda=632.8$ nm, and a primary particle size of 30 nm. The results are calculated at 1° intervals.

4.1. *Spheres*

For the ideal detection system consisting of an infinitesimal detector and collection of scattered light from $\theta=0$ to 2π, we find from equation (19) that σ_t can be obtained from F via the following equation

$$\sigma_t=\frac{2\pi DF}{E_0 a_1 \,dy\,dz}. \quad (36)$$

To provide an additional test of the radiometric model, we compare σ_t obtained from equation (36) with the exact value σ_s obtained from Mie theory. The results are summarized in Table 1 for the case of an infinitesimal detector located 1 cm from the laser beam and with a cell length L equal 690 cm. The cell length was taken to be six times larger than the nominal length in this comparison so that the angle range, $0.2°\leqslant\theta\leqslant179.8°$, approaches 0–180°. The error is at most 0.7% for particle sizes up to 2.35 μm, increases to 2.6% for the 4 μm particle size, and then to 4.8% for the 8 μm particle size. Further increases in the length produce only slight improvements. The major cause of discrepancy for the largest particles is that the scattering calculations are carried out at 1° increments. The actual error in the flux calculations for the various designs of the TCRN will be considerably less, at least a factor of 3 less, since the cell length is fixed at 115 cm.

We have exercised the model for a range of detector diameters, $DC=2.7$, 1.3 and 0.43 cm, the first two of which correspond to the dimensions of the cosine-corrected sensors studied experimentally. This allows an estimation of the effect of the finite detector size on the results. For each value of DC, the calculations were performed for four values of D: 6.85, 4.43, 2.38, and 1 cm. The first three correspond to the range examined experimentally and the fourth to a limiting case. Performing calculations for differing Ds allows one to estimate the effect of the angle truncation. In these calculations, the number of x elements I_m typically equals 300 and the number of sectors of the detector is typically 144 with $J1_{max}=12$.

The effect of angle truncation is illustrated in Fig. 7 for the case of fixed detector diameter, $DC=0.43$ cm, and values of D from 1 to 6.85 cm, which correspond to the smallest scattering angles θ_{min} of 1–6.8°. Here we plot the ratio of the simulated value of the total scattering cross-section σ_t to the value computed from Mie theory, σ_s. For the 6.8° truncation angle, the error is about 20% for the 2.35 μm sphere size, while for the 1° truncation angle, the error is about 2%.

The role of the finite detector size is assessed by comparing the simulated and predicted (Mie theory) total scattering for the three different detector diameters for a value of D equal to 1.0 cm, which corresponds to a smallest scattering angle, $\theta_{min}=1°$. The results are summarized in Fig. 8. The largest detector underestimates the total scattering intensity by about 20% for the smallest particle size and even exceeds the theoretical value by about 2% for $D=0.60$ μm. For

Table 1. Comparison of exact and model prediction for σ for polystyrene spheres

Sphere diameter (μm)	Mie theory σ_s (nm^2)	Model* σ_t (nm^2)	|Error|† (%)
0.0175	1.165×10^{-2}	1.165×10^{-2}	<0.1
0.234	2.113×10^{4}	2.114×10^{4}	<0.1
0.305	8.058×10^{4}	8.056×10^{4}	<0.1
0.60	1.089×10^{6}	1.088×10^{6}	<0.1
1.101	2.361×10^{6}	2.355×10^{6}	0.3
2.35	1.013×10^{7}	1.007×10^{7}	0.6
4.0	3.303×10^{7}	3.388×10^{7}	2.6
8.0	1.054×10^{8}	1.003×10^{8}	4.8

* $0.2^\circ<\theta<179.8^\circ$.
† $|\text{Error}|=|(\sigma_s-\sigma_t)/\sigma_s|$.

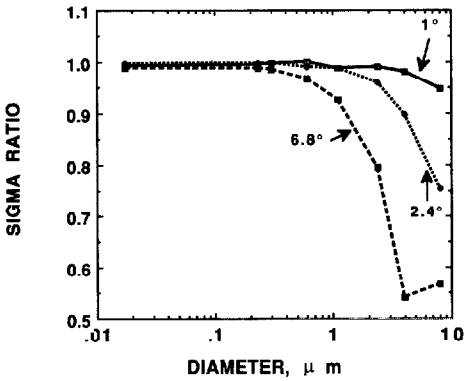

Fig. 7. Effect of angle truncation on the predicted TCRN performance, σ_t/σ_s, vs particle size of polystyrene spheres for D values of 6.85 cm ($\theta_{min}=6.8^\circ$), 2.38 cm ($\theta_{min}=2.4^\circ$), and 1.0 cm ($\theta_{min}=1^\circ$) for the case DC equals 0.43 cm and cell length, L, equals 115 cm. The angle θ_{min} equals $\tan^{-1}(2D/L)$ and is the smallest scattering angle for the cell.

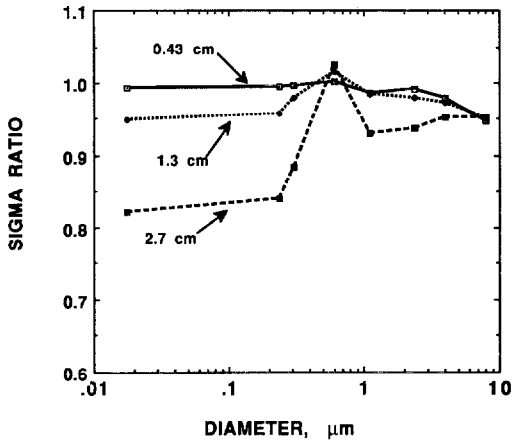

Fig. 8. Effect of finite detector size on predicted TCRN performance, σ_t/σ_s vs particle size of polystyrene spheres for DC values of 0.43, 1.3, and 2.7 cm for $D=1.0$ cm (θ_{min} equal 1°) and cell length equal 115 cm.

the smallest detector, the ratio is close to unity over the entire range.

The results for all the combinations of detector sizes and distances are summarized in Table 2 in terms of the particle size range for which the errors are less than 2, 5 and 20%. From Table 2 it is apparent that there are two constraints for obtaining accurate results. The most significant constraint is that there be a wide enough angular integration range. The larger the particle size the smaller the value of θ_{min}, which means a small value of D. For example, to obtain 5% uncertainty in the measurement of σ_t for an 8.0 μm sphere, requires $\theta_{min}=1.0$ ($D=1.0$ cm for a 115 cm long cell) and $DC=1.3$ or smaller. The second constraint is that the cosine sensor diameter, DC, be comparable to the distance D or smaller to minimize the error associated with the finite size of the detector. For $DC/D\leqslant1.25$, the finite-size-effect error is less than 5%, and for $DC/D\leqslant0.55$, the error is less than 2%.

4.2. *Agglomerates*

The exact results for the total scattering cross-section as a function of agglomerate size are obtained from equation (34). In Table 3 the radiometric model results for an infinitesimal detector area, $D=1$ cm, $L=115$ cm, and the length divided up into 300 increments are compared with the exact results. The properties of the agglomerates are as described above. In evaluating A given in equation (33), the refractive index, m, is taken to be $1.7-0.68i$. The polarizability is obtained from the Clausius–Mosotti relation

$$\alpha=\frac{3v_0}{4\pi}\left(\frac{m^2-1}{m^2+2}\right). \tag{37}$$

The difference between the exact result and the predicted instrument response is $\leqslant0.5\%$ for agglomerates with up to 10^4 primary units ($R_g=1.4$ μm). The increasing discrepancy for larger agglomerates is a result of the increasing fraction of the total scattering occurring for angles outside the detector's range ($D=1$ cm corresponds to detector's scattering range from 1.0 to 179.0°).

Table 2. Particle diameter range (μm) of polystyrene spheres for specified error limits for perfect cosine sensor

D (cm)	Error (%)	Diameter of detector, DC 2.7 cm	1.3 cm	0.43 cm
6.85	2	$\leqslant 0.31$	$\leqslant 0.31$	$\leqslant 0.31$
$\theta_{min} = 6.8°$	5	$\leqslant 0.6$	$\leqslant 0.6$	$\leqslant 0.6$
	20	$\leqslant 1.1$	$\leqslant 1.1$	$\leqslant 1.1$
4.43	2	$\leqslant 0.6$	$\leqslant 0.6$	$\leqslant 0.6$
$\theta_{min} = 4.4°$	5	$\leqslant 1.1$	$\leqslant 1.1$	$\leqslant 1.1$
	20	$\leqslant 2.4$	$\leqslant 2.4$	$\leqslant 2.4$
2.38	2	0.31–0.6	$\leqslant 0.6$	$\leqslant 1.1$
$\theta_{min} = 2.4°$	5	$\leqslant 2.4$	$\leqslant 2.4$	$\leqslant 2.4$
	20	$\leqslant 4.0$	$\leqslant 4.0$	$\leqslant 4.0$
1.0	2	None	0.6–2.4	$\leqslant 4.0$
$\theta_{min} = 1.0°$	5	0.6*	$\leqslant 8.0$	$\leqslant 8.0$
	20	$\leqslant 8.0$	$\leqslant 8.0$	$\leqslant 8.0$

* Only particle size for which error less than 5%.

Table 3. Comparison of exact and model calculation for σ for agglomerates

No. of spheres	R_g (μm)	D_s* (μm)	σ, equation (36) (nm^2)	σ_t, model (nm^2)	|Error|† (%)
10	0.040	0.065	1.522×10^3	1.522×10^3	<0.1
10^2	0.13	0.14	8.871×10^4	8.871×10^4	<0.1
10^3	0.45	0.30	2.457×10^6	2.456×10^6	<0.1
10^4	1.5	0.65	4.329×10^7	4.312×10^7	0.4
10^5	5.1	1.4	6.108×10^8	5.942×10^8	2.7
10^6	17	3.0	7.704×10^9	6.807×10^9	11.6
10^7	57	6.5	9.120×10^{10}	6.975×10^{10}	23.5

* D_s is the volume equivalent sphere diameter.
† $|\text{Error}| = |(\sigma - \sigma_t)/\sigma|$.

In carrying out the light scattering calculations for the agglomerates, it was found that a larger grid could be used because of the nearly monotonic character of the scattering function. Typically, 10 circular rings (100 sectors) were used and 100 increments in the x direction were used for the agglomerates compared to 12 circular rings (144 sectors) and 300 increments in the x direction for the spheres.

In Figs 9 and 10, we indicate in a manner analogous to the sphere results the effect of the angle truncation and finite size of the detector on the ratio of the simulated values for the total scattering coefficient to the exact results obtained from equation (34). The curves are qualitatively similar to those in Figs 7 and 8. The effect of the finite size of the detector seems to be more pronounced for the agglomerates than for the spheres. For $DC/D \leqslant 0.80$, the finite-size-effect error is less than 5%, and for $DC/D \leqslant 0.45$, the error is less than 2%. The results for all the combinations of detector sizes and distances are summarized in Table 4 in terms of the agglomerate size range for which the errors are less than 2, 5 and 20%.

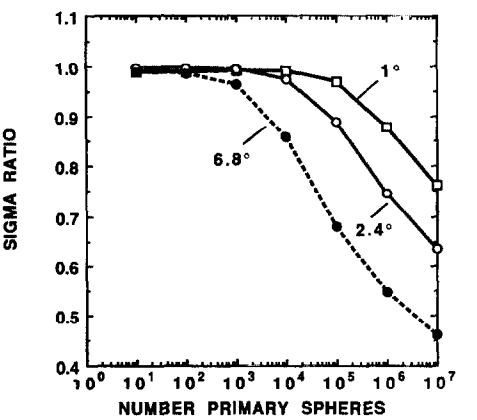

Fig. 9. Effect of angle truncation on the predicted TCRN performance, σ_t/σ_{ag}^t, vs number of primary spheres in the smoke agglomerate for D values of 6.85 (6.8°), 2.38 (2.4°), and 1.0 (1°) for the case DC equals 0.43 cm and cell length equals 115 cm.

5. PHYSICAL COSINE-CORRECTED SENSOR

The analysis up to this point is based on an ideal cosine sensor. This means that the light flux detected by the sensor is proportional to the product of the light intensity, incident on the sensor and the cosine of the angle ϕ defined by the scattering direction and the normal to the detector surface. As mentioned earlier, an aperture has a perfect cosine response since the flux

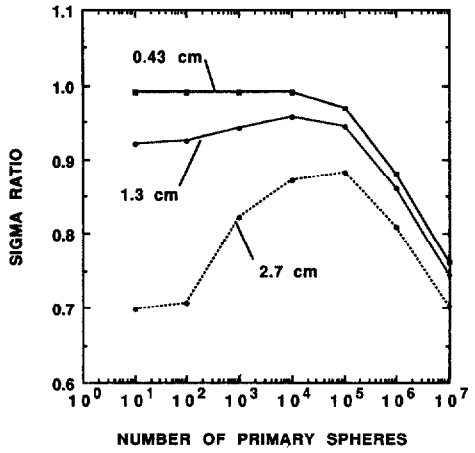

Fig. 10. Effect of finite detector size on predicted TCRN performance, σ_t/σ_{ag}^t, vs the number of primary spheres in the smoke agglomerate for DC values of 0.43, 1.3, and 2.7 cm for $D=1.0$ cm (θ_{min} equal 1°) and cell length equal 115 cm.

Table 4. Cluster size range (No. of primary spheres) for specified error limits for perfect cosine sensor

D (cm)	Error (%)	Diameter of detector, DC 2.7 cm	1.3 cm	0.43 cm
6.85	2	$\leqslant 10$	$\leqslant 10^2$	$\leqslant 10^2$
$\theta_{min}=6.8°$	5	$\leqslant 10^3$	$\leqslant 10^3$	$\leqslant 10^3$
	20	$\leqslant 10^4$	$\leqslant 10^4$	$\leqslant 10^4$
4.43	2	None	$\leqslant 10^3$	$\leqslant 10^3$
$\theta_{min}=4.4°$	5	$\leqslant 10^3$	$\leqslant 10^3$	$\leqslant 10^3$
	20	$\leqslant 10^4$	$\leqslant 10^4$	$\leqslant 10^4$
2.38	2	None	$\leqslant 10^3$	$\leqslant 10^3$
$\theta_{min}=2.4°$	5	10^3*	$\leqslant 10^4$	$\leqslant 10^4$
	20	$\leqslant 10^5$	$\leqslant 10^5$	$\leqslant 10^5$
1.0	2	None	None	$\leqslant 10^4$
$\theta_{min}=1.0°$	5	None	$\leqslant 10^4$	$\leqslant 10^5$
	20	10^3–10^6	$\leqslant 10^6$	$\leqslant 10^6$

* Only cluster size for error less than 5%.

entering the aperture is proportional to the projected area which, in turn, is proportional to cos ϕ. Once the aperture is covered with a transparent or translucent material such as glass, the flux of light penetrating the glass and passing through the aperture is no longer simply proportional to the cos ϕ. At each angle, some fraction of the light is reflected in addition to being diffracted with an increasing fraction being reflected as the angle ϕ approaches 90°. To compensate for this effect, a physical cosine-corrected sensor is a three-dimensional device. In this section, we briefly describe the cosine sensors used in the TCRN and present a model for the physical cosine sensor used in the radiometric transfer analysis. The idea here is to capture the essence of the physical sensor rather than making an exact mathematical model.

Two schematic designs of physical cosine sensors together with a truncated cone model of one of the sensors are shown in Fig. 11. Sensor I, obtained from EG&G,† contains a polytetrafluoroethylene (PTFE) membrane roughly in the shape of a truncated cone. The membrane acts as a diffuser with about 5% of the incident light transmitted through the membrane at normal incidence. Sensor II utilizes a 1.3 cm diameter diffuser and a stepped outer plate to obtain a cosine response. The dimensions of the stepped plate are based on the plate design reported by Schotland and Copp (1980). In both cases, the sensor is attached to a photomultiplier tube via an approximately 5 cm long, 2.5 cm diameter blackened tube.

Figure 12 shows good agreement between the perfect cosine response and our measured response for Sensor I up to angles of 85° for the case where the entire sensor area is uniformly illuminated. In Fig. 13 we show the angular response for the nominal 1 mm diameter laser beam incident on the center of the sensor. A constant response independent of the angle ϕ is expected in this case for a perfect cosine sensor, since the beam is not truncated by the area of the detector. The decreasing response with respect to angle is a result of an increased amount of reflection.

The mathematical model for sensor I is based on a truncated cone geometry as illustrated in the center of Fig. 11. The flat portion of the cone with a diameter of 2.7 cm is divided into 12 circles with 144 sectors. Three rings are on the sloped portion, and the number of sectors for ring N equals $2N-1$, just as for the circular region. The spacing of the rings is determined by the constraint that all sectors have equal area.

In computing the light flux from an element of the laser beam to an element of the sensor, we use the following power law approximation to the measured response function plotted in Fig. 13

$$H(\phi)=[1-(\phi/88.2)^2]^{0.4}, \quad \phi \leqslant 81$$
$$H(\phi)=0, \quad \phi>81. \tag{38}$$

This function replaces the cos ϕ in equation (9), which is correct only for the case of a perfect cosine sensor.

In the case of the circular sensor, some of the light scattered from every point along the laser beam reaches every point on the sensor's surface. This is not the case for the conical surface for two reasons. First, the scattering vector can be intercepted by one detector element before reaching a second as illustrated in Fig. 14. This case would correspond to an angle ϕ greater than 90°. The program for computing the total flux calculates cos ϕ from the dot product of the unit vector in the scattering direction, v, and N, the

† Certain commercial equipment, instruments, or materials are identified in this paper to specify adequately the experimental procedure. Such identification does not imply recommendation or endorsement by the National Institute of Standards and Technology, nor does it imply that the materials or equipment identified are necessarily the best available for the purpose.

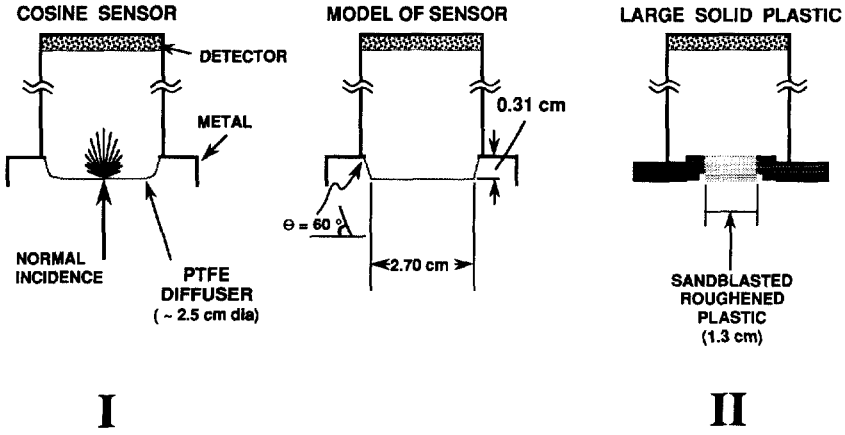

Fig. 11. Schematics of sensor I, sensor II, and a geometric representation of sensor I used in modeling the sensor performance.

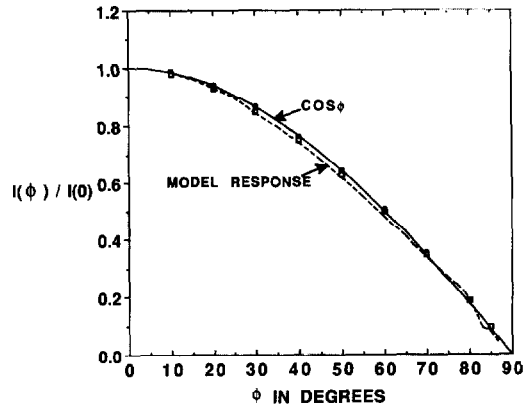

Fig. 12. Comparison of measured and model response of sensor I to a large beam of light that fills the entire detector area with uniform illumination. The symbols correspond to repeat measurements of the intensity vs angle ϕ. The solid curve corresponds to perfect cosine response.

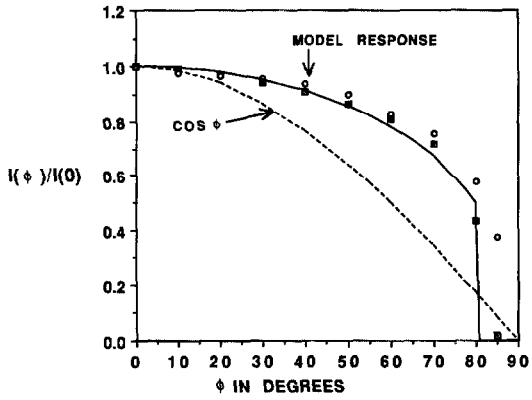

Fig. 13. Comparison of the measured response for sensor I and the model response of sensor I, to a small (laser) beam of light. The curve for perfect cosine response is also included.

unit normal to the detector surface.

$$\cos\phi = v \cdot N. \tag{39}$$

If $\cos\phi < 0$, which is equivalent to $\phi > 90°$, the program eliminates this term from the sum given by equation (9).

Secondly, for small scattering angles, the scattered light can be blocked by the "ears" from reaching the detector as illustrated in Fig. 14. The "ears" are designed to limit the range of scattering angles reaching the detector to 0–180°. In carrying out the total flux calculations, there is a check to see if the scattered light is intercepted by the "ears".

To test our computer program, we computed the light flux from a point source located far from the detector (10 cm). First we found that the computed intensity agreed within $\pm 1\%$ with a cosine response for a circular detector. Then the program was applied to the physical cosine corrected sensor with equation (38) replacing $\cos\phi$ in computing the radiant flux to the detector, and good agreement was obtained between experiment and the model results over the angle range of the measurements as shown in Fig. 12.

The model was developed based on measurements with a conical sensor. The cosine response was not measured by us for the solid plastic sensor, though Schotland and Copp indicate less deviation from perfect cosine response than we obtained for the conical shaped sensor. In the analysis below, we use the physical model based on the conical shape for both sensors.

We applied the physical cosine sensor model in computing the light scattered from the polystyrene spheres in essentially the same way as for the perfect cosine sensor. The ratio of the total flux to σ_s was computed for each particle size. The ratio is multiplied by a normalization factor, which makes the sigma ratio equal to unity for the smallest particle size. In general, there is agreement within 5% between the physical and perfect cosine sensor for the case of large

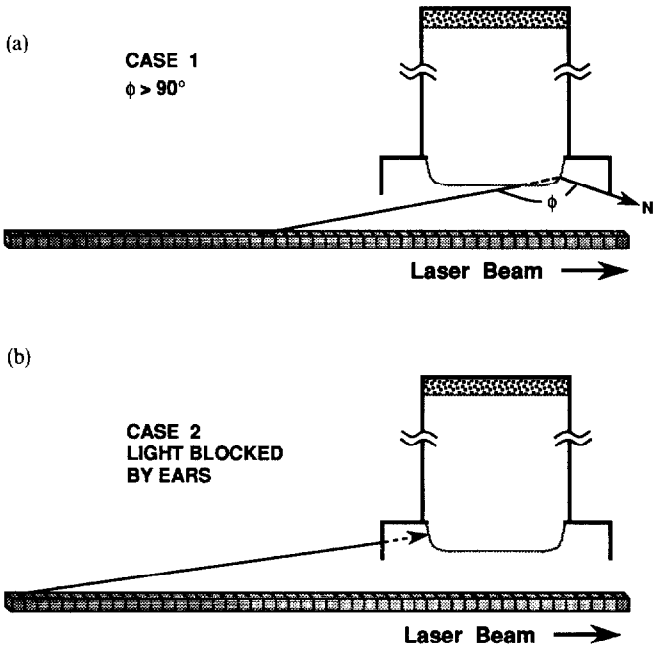

Fig. 14. Illustration of two unphysical conditions which must be checked for each radiant flux calculation for the physical cosine sensor (a) $\phi > 90°$ and (b) blockage by "ears".

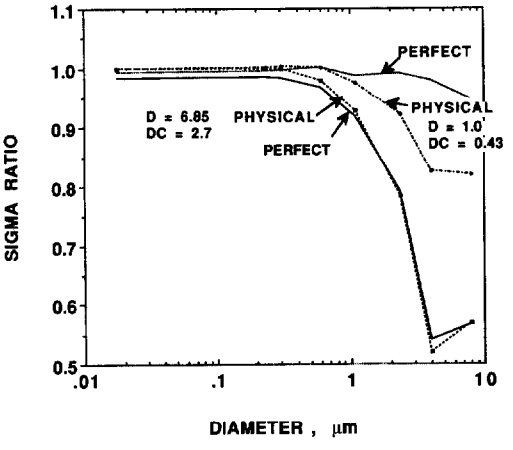

Fig. 15. Comparison of performance of "physical" and perfect cosine sensor for large ($D = 6.85$ corresponds to $\theta_{min} = 6.8°$) and small truncation angles ($D = 1.0$ corresponds to $\theta_{min} = 1°$) for polystyrene spheres. The symbols correspond to the computed points for the "physical" sensor.

truncation angle, $> 5°$. For small truncation angles there is a large difference between the two for large particle sizes as illustrated in Fig. 15. The difference is primarily a result of the response of the physical sensor for small angles. Large fractional errors in the cosine response for the model are evident in Fig. 12. The larger the particle size the more important that the cosine response be valid at ever smaller angles. No attempt was made to make the model give cosine response at arbitrarily small angles. Rather, the model was designed to agree with measured values for scattering angles as small as 5° (ϕ up to 85°).

6. EXPERIMENTAL RESULTS

Here we provide a brief account of the experimental procedure and the results. A complete description of the instrumentation and its performance is intended for a separate publication. An aerosol of polystyrene spheres was produced by atomizing a suspension of polystyrene spheres in filtered, deionized water. The liquid droplets produced by the atomizer evaporate as they pass through a diffusion drier leaving primarily individual polystyrene spheres. Dilution and passage through a mixing chamber further insure the droplets have evaporated before entering the TCRN (see Fig. 16). The concentration of the polystyrene suspension was adjusted so that the laser intensity typically decreased by 3–8% on passing through a 1.15 m cell. The following particle diameters were used: 0.100, 0.234, 0.305, 0.60, 1.101, and 2.35 μm. This general procedure is widely used in the aerosol community for producing monodisperse aerosols (Raabe, 1976) for calibration.

The TCRN measurements include the incident and transmitted laser intensity using photodiode detectors and the scattered light intensity with a cosine sensor followed by a Hamamatsu R-955 9-stage photomultyplier tube operating at 1000 volts. The photomulti-

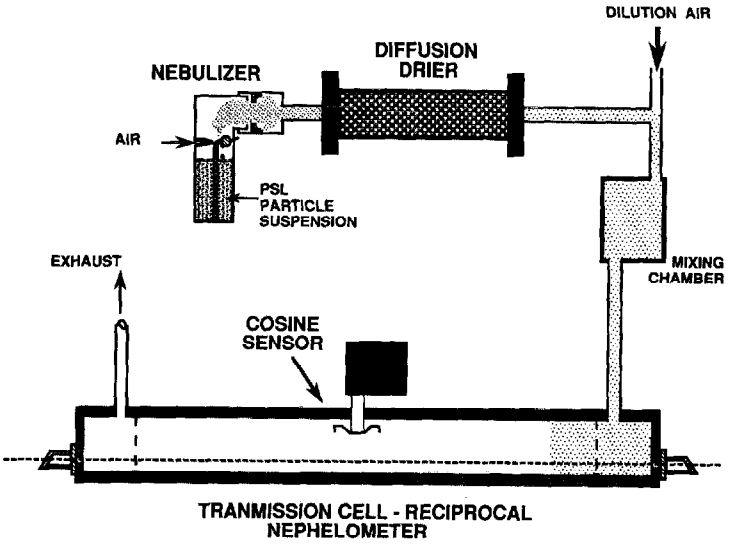

Fig. 16. Schematic of experimental setup for testing the TCRN performance with monosize polystyrene spheres. The cell is just starting to be filled as indicated by the dots.

plier (PM) output is integrated with a simple RC circuit with a 100 ms time constant. The analog signals from the two photodiodes, the PM tube, and the ratio circuit which computes the ratio of the two photo-diodie outputs, are converted to digital signals, which are read and stored every 5 s by a computer/data acquisition system. Typically a 10-point average is used in analysing the data. A measurement sequence consists of background measurements with filtered air, measurements of the polystyrene sphere aerosol for sensor I at a fixed position, measurements with the cosine sensor moved to a second and third position, and then remeasured with clean air to check for background drift. This sequence of measurements was performed for each of the particle sizes during a single day and a repeat measurement was typically performed for one particle size. Also, the entire series of measurements were repeated on a second day. A similar set of measurements was performed with the smaller cosine sensor.

For each set of measurements, the light extinction coefficient was computed using the Beer–Lambert law

$$\sigma_{ext} = \frac{\log(I_0/I)}{L} \tag{40}$$

where L is the optical pathlength in the cell, 115 cm. The quantity I_0 is measured as the ratio of the transmitted to incident laser intensity with no aerosol present and the quantity I is measured as the same ratio with the aerosol present. The reduced photomultiplier output is computed as

$$R = \frac{V_{PM}}{I_a \sigma_{ext}} \tag{41}$$

where V_{PM} is the output voltage of the photomultiplier tube minus the background voltage corresponding to no aerosol present and I_a is the incident laser beam intensity.

While there has not been a detailed evaluation of the linearity of the detectors, a preliminary series of measurements based on using three neutral density filters spanning a six-fold intensity range indicated that the detector outputs deviated from the linear response by 3% at most. The major source of measurement uncertainty for low aerosol concentrations arises from the background drift in the intensity ratio, typically about 0.05%. For the largest particle sizes, 1.101 and 2.35 μm, the aerosol concentration was low because of the difficulty of atomizing large spheres and the resulting extinction coefficients were about 0.025 m^{-1} for the 1.101 μm spheres and about 0.015 m^{-1} for the larger spheres. For these cases a background drift in the intensity ratio of 0.05% results in $\approx 2\%$ change in σ_{ext} for the 1.101 μm spheres and $\approx 3\%$ change for the 2.35 μm spheres. For the smaller sphere sizes, σ_{ext} was in the range 0.035–0.07 with an error less than 1% resulting from the background drift. Repeat measurements for σ_{ext} and R typically agree within 2% while day-to-day variation is typically less than 4% for the smaller particle sizes. An overall estimate of the measurement precision for aerosols with $\sigma_{ext} \geqslant 0.03$ m^{-1} is $\pm 4\%$ of the mean value at the 95% confidence interval (2σ).

For an ideal TCRN, the quantity R would be a constant for non-absorbing spheres such as polystyrene spheres, since both the numerator and denominator are proportional to the total scattering coefficient. In Figs 17 and 18, we see general agreement between the experimental results for the reduced R and the model predictions of the physical cosine sensor. Both the

measured and predicted results show less effect of particle size on response for the detector closer to the laser beam. The measured results for R for the largest particle size have the largest uncertainty both because of the low extinction coefficient and because of particle sedimentation. A 15% decrease in the light extinction coefficient was measured for the 2.35 μm spheres over a 60 s period starting 120 s after the aerosol was collected in the cell. The nominal residence time in the TCRN is about 90 s.

There seems to be a systematic decrease in R for the 0.305 μm spheres and a systematic increase for both sensors for $D = 6.85$ cm for the 0.60 μm spheres. The decrease in the case of the 0.305 μm spheres may be a result of the larger extinction coefficient for this particle size as discussed in the next section. We do not have an explanation for the systematic increase at 0.60 μm.

The finite-size-effect can be seen best by plotting the product of the PM output times the distance from the cosine sensor. According to equation (19), the product of radiant flux and D should be a constant if there were no finite-size-effect. As seen in Fig. 19, the measured finite-size-effect is about 5% for the 1.3 cm detector and about 14% for the 2.7 cm detector compared to predicted values of about 3 and 7%, respectively, for both detectors positioned closest to the laser beam.

7. DISCUSSION

This study represents the first quantitative modeling for the TCRN. However, there have been a number of calculations of the effect of angle truncation on the performance of the standard nephelometer (Ensor and Waggoner, 1970; Fitzgerald, 1977; Hasan and Lewis, 1983; Sloane *et al.*, 1991). Most of these studies have focused on the performance of commercially available nephelometers, the Meteorology Research Inc. (MRI) 1560 and 1590. These are widely used in ambient air quality monitoring, and the current version is manufactured by the Belfort Instrument Company.The nominal angle range for this instrument is 8–170°. In their studies of angular truncation errors, Fitzgerald (1977) and Sloane *et al.* (1991) found pronounced oscillatory behavior in the correction factor for monodisperse aerosols with particle diameters larger than about 2 μm for an angular integration range from 8 to 170°. A similar effect would be expected in our Fig. 7 for $D = 6.85$ if the sigma ratio were computed for more particle sizes in the range

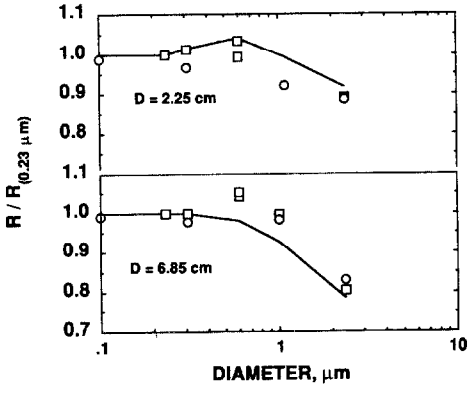

Fig. 17. Comparison of measured and predicted behavior (solid line) of TCRN, R/R (0.234 μm), as a function of particle size for the 2.7 cm diameter PTFE sensor (sensor I) positioned 2.25 cm (upper curve) and 6.85 cm (lower curve) from the laser beam. The different symbols correspond to measurements made on different days and the two square symbols for 0.6 μm spheres correspond to repeat measurements on the same day.

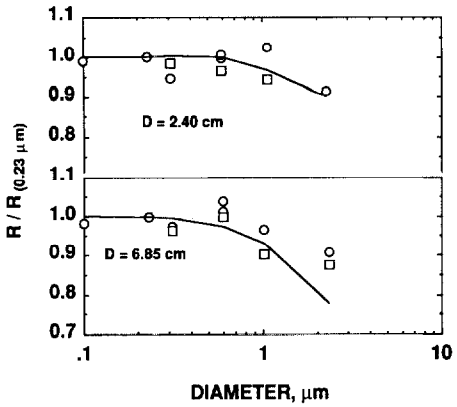

Fig. 18. Comparison of measured and predicted behavior (solid line) of TCRN, R/R (0.234), as a function of particle size for the 1.3 cm diameter sensor (sensor II) positioned 2.40 cm (upper curve) and 6.85 cm (lower curve) from the laser beam.

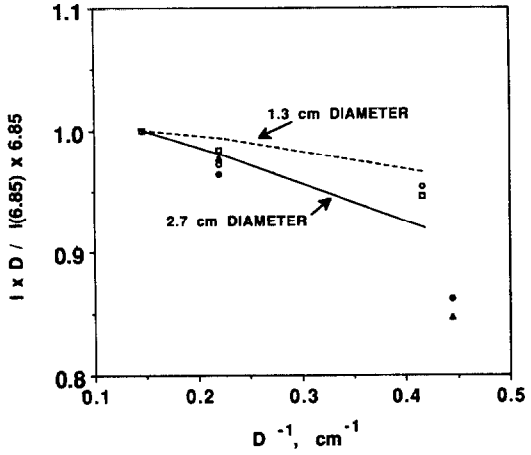

Fig. 19. Measured and predicted finite size effect for sensor I (solid symbols) and for sensor II (open symbols). Circles correspond to 0.100 μm spheres, squares to 0.234 μm spheres, and triangles to 0.305 μm spheres.

between 1 and 10 μm. There is an indication of the expected oscillatory behavior for the last two points. As indicated in Sloane *et al.* (1991), this oscillatory effect is less significant as the angle acceptance range increases. This oscillatory behavior, which becomes most evident for corrections on the order of 20% or more, suggests that the particle diameter range given in Table 2 may be overstated at least for the case of $D=6.85$ for 20% error.

The calculated results in this paper assume there is no attenuation of the laser beam. In reality the attenuation of the beam will result in a lower measured light scattering coefficient compared to the true value. We have carried out a series of calculations including the attenuation factor (see equation (5)) for light extinction coefficients equal to 0.01, 0.03 and 0.07 m^{-1}, for D_p of 0.0175, 0.60, and 8.0 μm, for $DC=2.7$ cm and for D equal to both 2.38 ($\theta_{min}=2.4°$) and 6.85 ($\theta_{min}=6.8°$). Over this range of parameters we find that the following expression agrees with the numerical result to within 0.1% for the ratio, R_a, of the light flux reaching the detector with beam attenuation included to the light flux without beam attenuation.

$$R_a=\exp(-k_{ext}L_a) \tag{42}$$

where

$$L_a=L/2+D. \tag{43}$$

As expected, this correction is most accurate for large particles where most of the light is scattered in the forward direction so that the pathlength of the light reaching the detector is close to the value given by equation (43), while the value is systematically high for the smallest particle size, since a significant fraction of the scattered light comes from back scattering with a resulting longer pathlength. For our experiments, the correction is largest for the 0.305 μm spheres, for which $\sigma_{ext}=0.07\ m^{-1}$ and $R_a=0.959$ (equation (42)). This may account for the lower value for R in the plots given in Figs 17 and 18 for the 0.305 μm spheres. If the value of σ_{ext} increases beyond 0.07 m^{-1}, multiple scattering will become more important and affect the accuracy of the measurements. There is a need to extend the model presented here to quantify the effect of multiple scattering on the measurement of σ. We expect the multiple scattering to be less significant for smoke agglomerates, since more of the light is absorbed than scattered.

A significant issue in the present study is the effect of finite size of the detector on the instrument performance; there has been no parallel study in the case of the standard nephelometer. We make a rough estimate of the finite-size-effect for the 1590 Model Nephelometer based on the diameter of the light diffuser, 1.9 cm, and the distance from the diffuser to the center of the detection cone, 3.2 cm. We estimate the finite-size-effect for the standard nephelometer to be on the order of 1% for spherical particles and about 2% in the case of agglomerates. The estimate is based on the performance of the TCRN for approximately the same value of the ratio DC/D.

There is a tradeoff between finite-size-effects and angle truncation. The closer the cosine sensor is to the light beam, the smaller the angle truncation error is but the larger the finite-size-effect error. There are situations such as in the measurement of optical properties of larger particles where it is advantageous to move the detector close to the beam. The finite-size-effect error is smaller for large particle sizes than for small ones because the increased forward scattering results in a larger effective scattering pathlength for the larger particles. For example, for the 1.3 cm diameter detector 1 cm from the beam, the error predicted by the radiometric model is less than 2% for particle size in the range 0.6–2.35 μm but increases to 5% for 0.0175 μm diameter spheres.

A major advantage of the TCRN over the standard nephelometer is the capability of experimentally testing for errors associated with angle truncation and finite size by performing both a total scattering and a light extinction measurement within the same optical cell. The key quantity of interest is the ratio of the PM output to the light extinction coefficient (equation (41)). Our study show that this ratio can be measured to a precision of $\pm 4\%$ for σ_{ext} in the range 0.03–0.07 m^{-1}. The primary sources of imprecision in the current design are the background drift in the measurement of the ratio of incident to transmitted light, about 0.05%, and the drift in the PM tube response.

We find that for our TCRN design with a 1.3 cm cosine sensor positioned 2.4 cm from the detector ($\theta_{min}=2.38°$) all the measurements and the predicted values agree within $\pm 5\%$ for spherical particles with diameters $\leqslant 1.1$ μm. We estimate that a similar uncertainty would apply for agglomerates with up to about 3×10^3 primary spheres. This design is similar to the one used by Patterson *et al.* (1991), which had the same size sensor, a slightly larger minimum angle of 3° compared to 2.4°, and a slightly larger finite-size-effect resulting from the laser beam being 2 cm from the detector compared to 2.4 cm in our study. To maintain 5% uncertainty for spheres up to 8 μm and agglomerates up to 10^5 spheres, it is estimated that the response of the cosine sensor must be within a few percent of perfect ($\cos\phi$) for a scattering range from 1 to 179°.

Acknowledgements—This work was funded in part by Grant W-17,980 from the Life Sciences Division of NASA and was monitored by Dr Guy Fogleman. Marjorie McClain provided programming assistance. Comments made by Craig Bohren (Pennsylvania State University) were crucial to the analysis in Appendix A.

REFERENCES

Beutell R. G. and Brewer A. W. (1949) Instruments for the Measurement of the Visual Range. *J. Sci. Instrum.* **26**, 357–359.

Bohren C. F. and Huffman D. R. (1983) *Absorption and Scattering of Light by Small Particles*. John Wiley, New York.
Charlson R. J., Horvath H. and Pueschel R. F. (1967) The direct measurement of atmospheric light scattering coefficient for studies of visibility and pollution. *Atmospheric Environment* **1**, 469–478.
Drolen B. L. and Tien C. L. (1987) Absorption and scattering of agglomerated soot particulate. *J. Quant. Spect. Rad. Transfer* **37**, 433.
Ensor D. S. and Waggoner A. P. (1970) Angular truncation error in the integrating nephelometer. *Atmospheric Environment* **4**, 481–487.
Fisher M. E. and Burford R. J. (1967) Theory of critical point scattering and correlation. I. The Ising model. *Phys. Rev.* **156**, 583.
Fitzgerald J. W. (1977) Angular truncation error of the integrating nephelometer in the fog droplet size range. *J. appl. Met.* **16**, 198–204.
Foote P. D. (1916) Illumination from a radiating disk. *Bull. Bur. Stand.* **12**, 583–586.
Gerber H. E. (1979) Portable cell for simultaneously measuring the coefficients of light scattering and extinction for ambient aerosols. *Appl. Opt.* **18**, 1009–1014.
Gerber H. E. (1982) Simultaneous measurements of aerosol scattering and extinction coefficients in a multi-pas cell. In *Light Absorption by Aerosol Particles* (edited by Gerber H. E. and Hindman E. E.), pp. 231–241. Spectrum Press, Hampton, VA.
Hasan H. and Lewis C. W. (1983) Integrating nephelometer response corrections for bimodal size distributions. *Aerosol Sci. Technol.* **2**, 443–453.
Iskander M. F., Chen H. Y. and Penner J. E. (1989) Optical scattering and absorption by branched chains of aerosols. *Appl. Opt.* **28**, 3083.
Johnson D. W., Kilsby C. G., McKenna D. S., Saunders R. W., Jenkins G. J., Smith F. B. and Foot J. S. (1991) Airborne observations of the physical and chemical characteristics of the Kuwait oil smoke plume. *Nature* **353**, 617–621.
Mountain R. D. and Mulholland G. W. (1988) Light scattering from simulated smoke agglomerates. *Langmuir* **4**, 1321–1326.
Nelson J. (1989a) Fractality of sooty smoke: implications for the severity of nuclear winter. *Nature* **339**, 611.
Nelson J. (1989b) Test of a mean field theory for the optics of fractal clusters. *J. mod. Opt.* **36**, 1031.
Patterson E. M., Duckworth R. M., Wyman C. M., Powell E. A. and Gooch J. W. (1991) Measurement of the optical properties of the smoke emission from plastics, hydrocarbons, and other urban fuels for nuclear winter studies. *Atmospheric Environment* **25A**, 2539–2552.
Raabe O. G. (1976) The generation of aerosols of fine particles. In *Fine Particles Aerosol Generation, Measurement, Sampling and Analysis* (edited by Liu B. Y. H.). Academic Press, New York.
Samson R. J., Mulholland G. W. and Gentry J. W. (1987) Structural analysis of soot agglomerates. *Langmuir* **3**, 272–281.
Schotland R. M. and Copp J. D. (1980) A narrow band spectral pyranometer. International Radiation Symposium, Volume of Extended Abstracts, pp. 562–564. Colorado State University, Fort Collins, CO.
Siegel R. and Howell J. R. (1981) *Thermal Radiation Heat Transfer*, p. 174. Hemisphere, New York.
Sloane C. S., Rood M. J. and Rogers C. F. (1991) Measurements of aerosol particle size: improved precision by simultaneous use of optical particle counter and nephelometer. *Aerosol Sci. Technol.* **14**, 289–301.

APPENDIX A

Calculation of $I_A + I_B$

The following expression relates the horizontal and vertical components of the scattered electric fields, E_h^s and E_v^s, to the incident fields.

$$\begin{pmatrix} E_h^s \\ E_v^s \end{pmatrix} = C \begin{pmatrix} S_2(\theta) & S_3(\theta) \\ S_4(\theta) & S_1(\theta) \end{pmatrix} \begin{pmatrix} E_h^i \\ E_v^i \end{pmatrix} \tag{A1}$$

where C is a coefficient independent of θ.

The horizontal and vertical planes are relative to the scattering plane, which is defined by the incident and scattering directions. For the upper point, A, the scattering plane is at an angle α from the horizontal (see Fig. 3). The components of the incident fields are given by

$$\begin{aligned} E_h^i &= E_0 \cos\alpha + E_0 \sin\alpha \\ E_v^i &= -E_0 \cos\alpha + E_0 \sin\alpha \end{aligned}, \text{ for point } A \tag{A2}$$

$$\begin{aligned} E_h^i &= E_0 \cos\alpha - E_0 \sin\alpha \\ E_v^i &= -E_0 \cos\alpha - E_0 \sin\alpha \end{aligned}, \text{ for point } B. \tag{A3}$$

The scattered field components are calculated from equations (A1)–(A3) and the intensity I_A at point A is computed from the fields as follows

$$I(A) = E_h^s E_h^{s*} + E_v^s E_v^{s*}. \tag{A4}$$

We obtain a similar expression for I_B. The sum $I_A + I_B$ reduces to the following expression in terms of the components of the Mueller Matrix

$$I_A + I_B = 4|C|^2 |E_0|^2 [S_{11}(\theta) - \cos(2\alpha) S_{13}(\theta)]. \tag{A5}$$

The quantity S_{13} vanishes for randomly oriented non-spherical particles that are superposable on their mirror image so that the final result is independent of α.